Modelling and experimental analysis of the effect of solute iron in thermally grown Zircaloy-4 oxides

Y. R. Than[a], M. R. Wenman[a], B. D. C. Bell[a], S. R. Ortner[b], H. Swan[b] and R. W. Grimes[a]

[a]Department of Materials and Centre for Nuclear Engineering, Imperial College London, London, SW7 2AZ, UK
[b]National Nuclear Laboratory, Culham Science Centre, Abingdon, Oxfordshire, OX14 3DB, UK

September 23, 2019

Abstract

Simulations based on density functional theory (DFT) were used to investigate the behaviour of substitutional iron in both tetragonal and monoclinic ZrO_2. Brouwer diagrams of predicted defect concentrations, as a function of oxygen partial pressure, suggest that iron behaves as a p-type dopant in monoclinic ZrO_2 while it binds strongly to oxygen vacancies in tetragonal ZrO_2. Analysis of defect relaxation volumes suggest that these results should hold true in thermally grown oxides on zirconium, which is under compressive stresses. X-ray absorption near edge structure (XANES) measurements, performed to determine the oxidation state of iron in Zircaloy-4 oxide samples, revealed that 3+ is the favourable oxidation state but with between a third and half of the iron, still in the metallic Fe^0 state. The DFT calculations on bulk zirconia agree with the preferred oxidation state of iron if it is a substitutional species but do not predict the presence of metallic iron in the oxide. The implications of these results with respect to the corrosion and hydrogen pick-up of zirconium cladding are discussed.

1 Introduction

Fuel cladding in water-cooled reactors should have high resistance to radiation damage, be relatively transparent to thermal neutrons, have good corrosion resistance and good mechanical properties. Zirconium alloys can be tailored to fulfil these requirements and thus are among the most commonly used materials for fuel cladding [1]. Nevertheless, zirconium alloys take-up hydrogen released during the corrosion process, leading to the formation of hydride precipitates, which are detrimental to cladding performance.

Both the rate of corrosion and the hydrogen pick-up fraction (HPUF) in nuclear fuel cladding have been linked to alloying content [2–4]. Commonly used alloys such as Zircaloy-2, Zircaloy-4, M5^{TM} and ZIRLO^{TM} include small amounts of iron as it has been shown to increase corrosion resistance [5]. Recent developments in zirconium alloys have been tending towards higher iron content, such as the HiFi (High corrosion resistance and high iron zirconium) alloy developed by Nuclear Fuel Industries Ltd., which demonstrate superior corrosion resistance (mainly in terms of nodular corrosion) [6]. Other reports also suggest that iron can also be beneficial to the general corrosion in zirconium alloys [7]. The addition of iron has also been shown to reduce the HPUF in zirconium alloys [8], whereas other authors report the opposite effect through a different mechanism [9, 10]. In the metal substrate, it is found that iron atoms are readily rejected from the matrix of zirconium alloys, forming secondary phase particles (SPPs) but also segregating to grain boundaries [11, 12]. The sizes and compositions of SPPs have also been linked to HPUF [9, 10, 13, 14]. Intermetallic Fe-Zr phases have also been characterised [15]. This analysis however focuses on the role of dissolved iron.

Hudson *et al.* [16] showed that precipitation and segregation left only between 0.003 at% and 0.018 at% iron in the matrix, in comparison with typical alloy compositions of about 0.3 at% in common cladding alloys [17]. Other authors have reported seeing regions with up to 0.42 at% iron in solution [18]. It has been shown that grain boundaries with high iron concentrations can continue uninterrupted for at least about 70 nm into the oxide, thus it may be possible to expect similar heterogeneous distributions of iron in the oxide [19]. During oxidation, the iron-containing SPPs show either simultaneous or delayed oxidation with respect to the matrix, depending on the type of precipitate [20]. This affects both the rate and level that the oxide is doped with iron.

Even when the SPPs are fully oxidized, not all the iron will be incorporated into the ZrO_2, as iron from oxidizing SPPs has been observed to diffuse towards free surfaces, forming an iron oxide phase on the outer surface of the oxide or on internal crack faces [21, 22]. Finally, radiation has a significant impact on the iron-containing SPPs, which have been shown to undergo amorphous transformation and also segregation and dissolution of iron into the matrix [23–28]. This may cause a greater amount of iron to be found in solid solution as compared with that observed for unirradiated material.

The mechanisms by which solute iron affects corrosion rate and HPUF can be associated with the substitution of iron ions on zirconium sites within the oxide layer and the resulting changes in defect populations. The charge states of oxidised iron are 2+ or 3+ in ZrO_2 [29–31], while that of zirconium is 4+, so charge neutrality must be achieved by a change in the defect population. For example, should compensation occur via an increase in the concentration of oxygen-site vacancies, and Kakiuchi *et al.* [8] have suggested that this would result in more active recombination of these vacancies with incoming oxygen anions at the surface. This, in turn, would mean that more electrons were consumed at the surface, making the electronic potential there higher, allowing electrons formed from

the oxidation of the metal to flow out more easily. This decreases the overall electrical potential gradient across the oxide, which should decrease the ingress of hydrogen into the metal [32, 33]. An increased oxygen vacancy concentration could also affect the corrosion rate via its stabilizing effect on tetragonal ZrO_2 [34] as some studies [35–37] suggest that the tetragonal-to-monoclinic phase change induces the transition from low to high corrosion rates. If so, suppressing the phase change would extend times between transitions and hence reduce the overall corrosion rate.

In this paper, the mechanisms by which iron affects the oxidation rate and hydrogen pickup rate of zirconium alloys are considered in the light of the defects produced by the dissolution of iron in ZrO_2. The effects of iron additions on the types of defects and their concentrations in ZrO_2 are investigated by carrying out density functional theory (DFT) simulations of iron defects in isolation and in clusters with other iron and intrinsic defects. The need to consider the effect of bound defects on oxidation state, defect populations and therefore overall oxide behaviour was shown by Bell *et al.* for both tin and niobium [38, 39]. It was shown for tin that including paired defects significantly increased the oxygen partial pressure at which the 2+ state was stable [39]. Paired defects in Zr-Nb alloys showed why niobium can exist in tetragonal ZrO_2 below the 5+ oxidation state and explained why X-ray absorption near-edge structure (XANES) measurements consistently showed 2+, 3+ and 4+ oxidation states [38]. Finally, the simulation results for iron are compared with XANES measurements of the oxidation state of iron within an oxide grown on Zircaloy-4.

2 Methodology

2.1 DFT

To understand the effect that alloying zirconium with iron has on the oxidation of zirconium alloys, defect formation energies in ZrO_2 are predicted using the DFT software CASTEP 8.0 [40]. These are used later to identify relative defect concentrations as a function of oxygen partial pressure.

Defects are modelled in both tetragonal ($P4_2/nmc$) and monoclinic ($P2_1/c$) ZrO_2 since both phases are found in the oxide layer of corroded zirconium alloys [41]. Defects are introduced into a perfect ZrO_2 supercell subject to periodic boundary conditions. To minimise defect image interactions across the periodic boundaries, a $2 \times 2 \times 2$ supercell is used for monoclinic ZrO_2 while a $3 \times 3 \times 2$ cell is used for the tetragonal phase [38]. The chosen supercell sizes offer an acceptable compromise between accuracy and computation time.

Throughout the DFT calculations, the Perdew-Burke-Ernzerhof (PBE) [42] exchange-correlation functional was employed. The pseudo-potential was generated from CASTEP version 6.0 for consistency and comparison with previous work. The plane-wave basis cut-off energy was 550 eV while the Brillouin zone sampling was carried out using the Monkhorst-Pack scheme [43]

with a k-point spacing of 0.045 Å^{-1}. The self-consistent field calculation for solving the Kohn-Sham equations employed Pulay's density mixing algorithm [44] with an energy convergence criteria of 10^{-8} eV. Geometry optimisation was considered to have converged when, between iterations, the energy difference is below 10^{-5} eV per ion, the maximum ion displacement is below 5×10^{-4} Å and the maximum force on each ion is not more than 0.01 eV/Å.

The defects considered were either: single substitutions, interstitials, vacancies, pairs of defects (clusters) involving an iron substituted at a zirconium site and an oxygen vacancy, or a trimer cluster consisting of two iron substitutional species (on zirconium sites) adjacent to an oxygen vacancy. For defects involving a single iron bonded to an oxygen vacancy, 2nd nearest neighbour positions were also considered as it has been shown in doped CeO_2 that the nearest neighbour configuration may not always have the lowest energy [45] (i.e. we do not discount the possibility). Charge states of 2+ and 3+ were considered for iron. Possible interstitial sites in both phases of oxide were considered using the Wyckoff positions of the relevant space groups.

The defect energies obtained from the DFT calculations were used to calculate formation energies of the defects with respect to the oxygen chemical potential based on an approach by Zhang and Northup [46], with the exception that a screened Madelung correction [47] was used instead of the Makov-Payne method [48] to account for defect self-interaction.

Essentially, the concentration c_i of a defect indexed i can be related to the Gibbs energy of the formation of the defect ΔG_i^f as

$$c_i \propto \exp\left(\frac{-\Delta G_i^f}{k_B T}\right) \tag{1}$$

where k_B is the Botlzmann constant and T is the temperature. At cladding operating temperatures, ΔG_i^f can be approximated by the formation energy ΔE_i^f,

$$\Delta E_i^f = E_{\text{def}}^{\text{DFT}} - E_{\text{perf}}^{\text{DFT}} + \sum_\alpha n_\alpha \mu_\alpha + q(E_{\text{VBM}} + \mu_e) + E_{\text{SM}} \tag{2}$$

where $E_{\text{def}}^{\text{DFT}}$ and $E_{\text{perf}}^{\text{DFT}}$ are the DFT calculated energies of the defective and perfect cells respectively, n_α is the number of atoms of species α added (or removed) in the formation of the defect, μ_α is the chemical potential of species α, q is the charge of the defect, E_{VBM} is the energy of the valence band maximum of the perfect cell derived from the DFT calculations, μ_e is the chemical potential of the electrons relative to E_{VBM} and E_{SM} is a screened Madelung correction (described in [47]) to account for defect self-interaction. Electron and hole concentrations (c_e and c_h) are also calculated as,

$$c_e = N_c \exp\left(\frac{-(E_g - \mu_e)}{k_B T}\right) \tag{3}$$

and

$$c_h = N_v \exp\left(\frac{-\mu_e}{k_B T}\right) \tag{4}$$

where N_c and N_v are the effective conduction and valence band density of states and E_g is the band gap of the perfect crystal. Boltzmann statistics are used here as ZrO_2 is insulating and thus the concentrations of the electrons and holes are expected to be low.

The values for μ_{Zr}, μ_{Fe} and μ_{O} can be determined as a function of P_{O_2} and T using DFT values as well as known values in standard conditions (method has been described in [49] with FeO being the reference oxide used for iron). μ_{Fe} will then be adjusted to ensure that the concentration of iron-containing defects reflect the predetermined amount of iron doping in the cladding material (note that due to this step, the results will not be sensitive to the reference oxide used for iron). The remaining unknown, μ_e, will be determined by imposing the overall charge neutrality of the system.

Brouwer diagrams were generated with concentrations from 10^{-5} to 10^{-2} units of iron per ZrO_2 to cover the range likely to be present due to local microstructural heterogeneity in the oxide formed from the depleted matrix, in regions near grain boundaries and from regions near SPPs. The values of the parameters and energies used in the generation of the diagrams are reported in Section 1 of the supplementary material.

The binding energies of clusters were calculated by taking the difference between the formation energy of a cluster and the sum of the formation energies of the individual components of the cluster. For example, the binding energy of a cluster formed by defects X and Y is given by

$$E^B_{\{X:Y\}} = E^f_X + E^f_Y - E^f_{\{X:Y\}} \tag{5}$$

where $E^f_{\{X:Y\}}$ is the formation energy of the cluster and E^f_X and E^f_Y are the formation energies of defects X and Y respectively. Thus, positive binding energies indicate favourable clustering. The defect clusters considered generally show positive binding energy, which is a necessary though not sufficient condition if the clusters are to be apparent in the Brouwer diagrams (as indeed they are).

Defect relaxation volumes allow us to consider the effects of stress in the oxide, which was not included in the DFT model but could have significant impact on defect concentrations in the real material. These provide an estimate of the change in volume of the supercell as a result of introducing a defect. The relaxation volume ΔV is calculated from,

$$\Delta V = -\frac{V}{3B}\,\mathrm{Tr}(\boldsymbol{\sigma}_{res}) \tag{6}$$

where V is the volume of the perfect supercell, B is the bulk modulus and $\boldsymbol{\sigma}_{res}$ is the 'residual' stress tensor for the converged supercell of the defect of interest. It is possible that in the real system (where the oxide is subject to a compressive stress), defects with negative relaxation volumes could be modestly more favourable than the equilibrium Brouwer diagrams suggest. This is because a negative relaxation volume will help to relieve the compressive stresses present in the oxide [33]. Nevertheless, a large positive or negative relaxation volume

implies a significant local elastic strain has been imparted with an associated energy penalty.

It is important to note here that the relaxation volumes obtained in this method (using constant volume calculations) may not necessarily produce reliable results for charged defects. Bruneval *et al.* have linked this to the different conventions imposed on the electrostatic potential [50], thus different DFT programs can give rather different values of ΔV. For reference, CASTEP uses a zero-average convention, ensuring that the average electrostatic potential over the cell is always zero. For relevant defects, another set of relaxation volumes have been obtained using constant pressure calculations, which has been shown to agree for CASTEP and the VASP program and therefore not convention dependent [51], to understand the impact of this error. The comparison between relaxation volumes obtained through both methods is reported in Section 2 of the supplementary material and it is found that the difference is small enough to have no significant impact on our analysis. Therefore we have chosen to continue using the relaxation volumes as obtained from equation (6) as the defect energies have been obtained from constant volume calculations as well.

It is also useful to calculate the volume change upon clustering. For defects X and Y, this volume change $\Delta V^c_{\{X:Y\}}$ is obtained by

$$\Delta V^c_{\{X:Y\}} = \Delta V_{\{X:Y\}} - \Delta V_X - \Delta V_Y \tag{7}$$

Should defects show negative $\Delta V^c_{\{X:Y\}}$ then clustering will be favourable under compressive stress. This is, however, an argument for the total system whereas locally any defect cluster with a large defect volume is subject to an elastic energy penalty, which will impact on its (relative) formation energy and hence its defect concentration.

2.2 XANES

The sample used for the X-ray absorption near-edge structure (XANES) measurements was a tile of Zircaloy-4 of composition within the range required by ASTM B353 (1.2-1.7 wt. % Sn, 0.18-0.24 wt. % Fe, 0.07-0.13 wt. % Cr, $<$ 70 wt. ppm Ni, $<$ 1600 wt. ppm O). This had been exposed to air at 900 K for 17 hours to produce a 25 μm thick oxide. A cross-section through the oxide and substrate was cut (see Figure 1), ground with silicon carbide and polished with increasingly fine diamond paste to a 1 μm finish. Measurements were performed on Beamline I18 at the Diamond Light Source (energy resolution Si 111, $\Delta E/E = 1.4 \times 10^{-4}$). X-ray fluorescence (XRF) maps were used to identify two locations in the oxide high in iron (i.e. incorporating oxidised SPPs near the polished surface); one near the metal-oxide interface and one near the oxide surface. XANES was performed at these two locations on the cross-section using a beam size of 5 μm $\times$ 5 μm. The detector was at 90° to the incoming beam, and the sample at 45° to both the incident and scattered beam. The iron K-edge is at 7112 eV, and the XANES measurements were obtained over an energy range of approximately -150 eV to 170 eV relative to this edge energy.

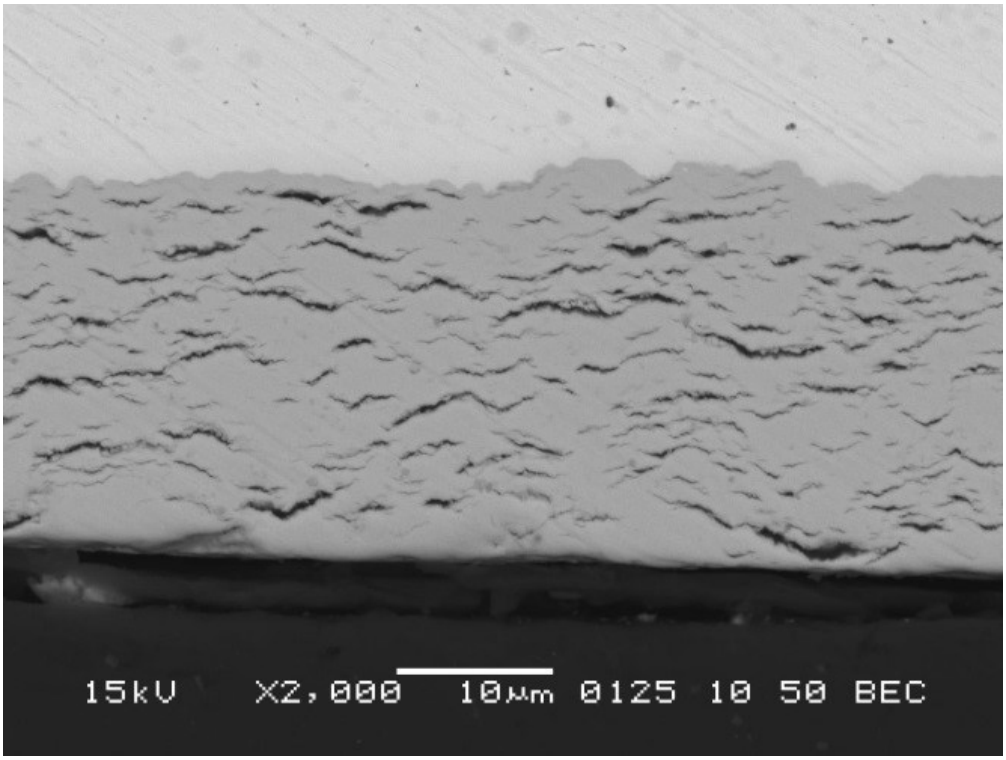

Figure 1: Cross section of thermally grown oxide. The three distinct layers are, from the top, the mounting medium, the oxide and the Zircaloy-4 metal.

XANES spectra obtained using fluorescence mode were normalised using:

$$\mu(E) = \left(\frac{I_f}{I_0}\right) \tag{8}$$

where $\mu(E)$ is the X-ray absorption, I_0 is the intensity of the incoming beam and I_f is the intensity measured in the fluorescence detector.

XANES measurements were also performed on the following standards: Fe (foil), FeO (powder) and Fe_2O_3 (powder), using 'transmission mode', again with a beam size of 5 μm $\times$ 5 μm. The XANES transmission spectra were normalised using:

$$\mu(E) = \ln\left(\frac{I_t}{I_0}\right) \tag{9}$$

where I_t is the intensity of the transmitted beam (using the ion chamber in the 'straight-through' position).

Data analysis was performed using the ATHENA software for X-ray absorption spectroscopy (XAS) data processing, which is now part of the package 'Demeter' [52]. The spectrum taken

from the iron foil was used for the calibration of the energy axis. Plotting the derivative of the absorption spectrum with respect to energy gave rise to two peaks of almost equal intensity (due to the pre-edge feature in the original spectrum). For this reason the second peak of the derivative function was selected as the edge energy, since this energy also corresponded to the position of the main increase in absorbance. This energy was calibrated to the known iron K-edge energy of 7112 eV (by using a value for 'Eshift' of -6.76 eV). This 'Eshift' value was also applied to the two sample datasets and the remaining data from the standards FeO and Fe_2O_3, producing the edge energies reported in Table 1.

The two spectra from the sample and the spectra from the iron foil, FeO and Fe_2O_3 standards were normalised using the parameters/energy ranges in Table 1 for the pre-edge and post-edge background subtraction. The results were not sensitive to the precise fitting ranges so long as the initial peak in the XANES spectrum was avoided, and the range was long enough to include several of the minor peaks at high energies.

Table 1: Edge energies and energy range parameters for the standards and sample data normalisation.

Sample	Edge Energy, E_0 (eV)	Pre-edge range fitting (eV relative to E_0)		Post-edge range fitting (eV relative to E_0)	
		Min	Max	Min	Max
Fe foil standard	7112	-150	-30	50	170
FeO standard	7115	-150	-30	30	160
Fe_2O_3 standard	7118.4	-150	-30	30	160
Zircaloy-4 oxide near M/O interface	7114.4	-150	-30	18	170
Zircaloy-4 oxide near oxide surface	7118.4	-150	-50	70	160

Linear combinations of the three spectra for the iron foil, FeO and Fe_2O_3 standards were fitted to the spectra from the Zircaloy-4 oxide. The energy range chosen for the fit was 20 to 30 eV, to include the XANES region only. These spectra, taken in fluorescence mode, have not been corrected for self-absorption; however, the atomic fraction of iron present is small enough that self-absorption corrections should not be required.

3 Results and Discussion

3.1 Brouwer Diagrams

Figure 2 shows the defect concentrations in intrinsic and iron-doped monoclinic ZrO_2 at 635 K, which is a typical temperature for autoclave experiments on zirconium cladding. For

the iron-doped case, the Brouwer diagram shown is for 0.01 at.% of iron in the cladding, which corresponds to 0.0001 units of iron per ZrO_2. Other concentrations demonstrate the same trends. It can be seen that for all oxygen partial pressures in iron-doped monoclinic

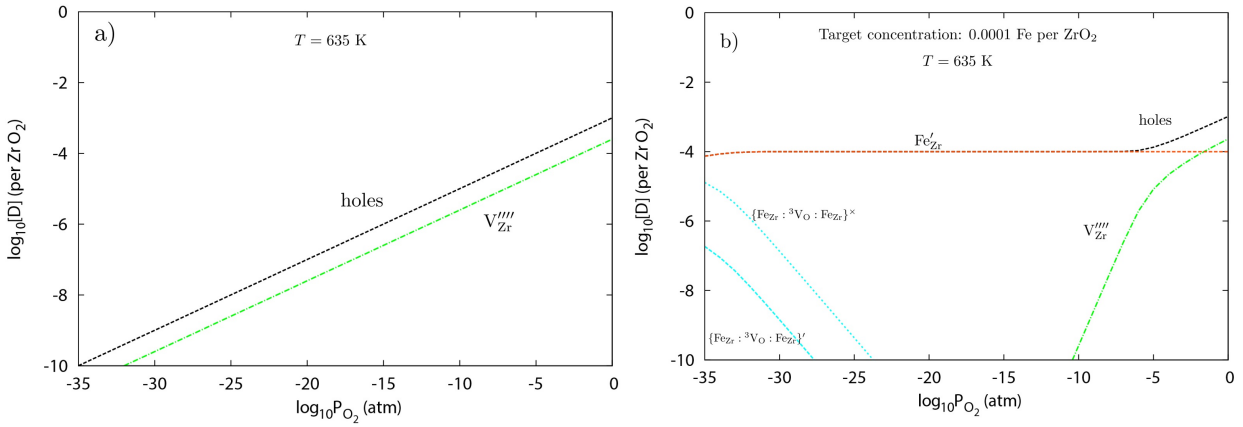

Figure 2: Brouwer diagrams showing defect concentrations in monoclinic ZrO_2 at 635 K as a function of oxygen partial pressure: a) ZrO_2 with no iron and b) 0.0001 units of iron per ZrO_2. ${}^3V_O$ refers to vacancies in the 3-coordinated oxygen sites. Defects with concentrations below 10^{-6} at all P_{O_2} are not shown.

ZrO_2, the preferred defect is Fe'_{Zr}; that is Fe^{3+} on a zirconium site charge compensated by holes. Compared to the undoped ZrO_2, there is a significant increase in the concentration of holes at lower oxygen partial pressures, which indicates that, in monoclinic ZrO_2, iron is acting as a p-type dopant. Possible consequences of this may be understood by looking at the behaviour of holes in monoclinic ZrO_2. The mobility of holes in monoclinic ZrO_2 is two orders of magnitude lower than that of electrons [53] and thus we expect electronic conduction to still be the dominant charge carrier. This is important as should holes be migrating instead, they would be unable to recombine and stop the influx of H^+ ions, leading to greater HPUF. Furthermore, it has been shown that the mobility of holes is much lower at surfaces than in the bulk, causing them to readily segregate to surfaces [54]. This would imply that the increase in hole concentration could lead to an increase in positive charge accumulation on surfaces such as grain boundaries, which may impede the ingress of H^+ into the oxide and thus lowering HPUF. Only at very low P_{O_2} does the concentration of some clustered defects start to become significant, but it is also the only instance where oxygen vacancies are present. (Note: Unpaired oxygen vacancies in both diagrams do form but have concentrations that are too low to appear in the diagram.) This suggests that in this phase, under very low P_{O_2} conditions, iron atoms cluster with oxygen vacancies, and that the presence of substitutional iron stabilises the presence of the oxygen vacancies.

For tetragonal ZrO_2, Brouwer diagrams (Figure 3) were generated at 1500 K since it is the temperature where this phase becomes stable without stress or doping. Previous stud-

ies [38, 49, 55, 56] using similar simulation techniques have also taken this approach and have generated results consistent with experiment. A Brouwer diagram was also generated at 900 K for comparison.

Comparing first the undoped (Figure 3a) and the iron-doped (Figure 3b) diagrams at 1500 K, doubly charged oxygen vacancies charge compensated by electrons are the dominant defect at low P_{O_2} with very similar concentrations in both cases. Equivalently at high P_{O_2}, holes compensating for fully charged zirconium vacancies dominate in doped and undoped materials. It is only at intermediate P_{O_2} that there is a difference with the $\{Fe'_{Zr} : V_O^{\bullet\bullet} : Fe'_{Zr}\}'$ cluster dominating in the doped case.

Figure 3b is consistent with the dominant iron defect, across all P_{O_2}, consisting of two substituted iron ions adjacent to an oxygen vacancy (i.e. a trimer). At higher P_{O_2}, both iron species prefer to be in the 3+ state, gradually shifting to a preference for 2+ as the environment becomes more reducing. A single Fe^{3+} ion paired to an oxygen vacancy (i.e. a dimer) trails by an order of magnitude in concentration across all P_{O_2} while an isolated Fe^{3+} is of minor significance even at the highest P_{O_2}. At this concentration of iron (10^{-4} iron per ZrO_2), the concentration of the (most favourable) trimer is roughly constant across the range of P_{O_2} studied.

Figure 3b predicts that most oxygen vacancies will remain unpaired at very low P_{O_2}, suggesting oxygen ion migration would not be affected by iron. This may not, however, necessarily hold true in a thermally grown oxide on zirconium cladding, as oxygen vacancies are only significant in Brouwer diagrams above 1000 K, which is significantly above the cladding operating temperature, or where locally, the iron concentration is much higher. To help illustrate these points, two further Brouwer diagrams were generated; Figure 3c where the temperature is reduced and Figure 3d where the concentration of iron is increased. Figure 3c shows the predicted defect concentrations for the iron doped tetragonal ZrO_2 at 900 K and it can be seen that across all P_{O_2}, oxygen vacancies now show a preference to be bound to iron atoms. The Brouwer diagrams also predict that this pairing of iron atoms with oxygen vacancies becomes more significant at low P_{O_2} when the concentration of iron is sufficiently high. This is also evident when comparing Figures 3b and 3d, where at low P_{O_2}, with higher concentration of iron, the concentration of paired iron defects becomes more significant in comparison to the dominant oxygen vacancies.

The strong preference of iron ions to cluster with oxygen vacancies predicted in this study suggests that iron could be binding the oxygen vacancies at key specific locations such as grain boundaries and the oxide-metal interface. This could be especially important in regions where iron content is higher. Thus, if the migration of O^{2-} ions through the oxide is primarily via an oxygen vacancy hopping mechanism, then migration could be significantly slowed when the iron content in the oxide is higher locally, which could lead to a reduced corrosion rate.

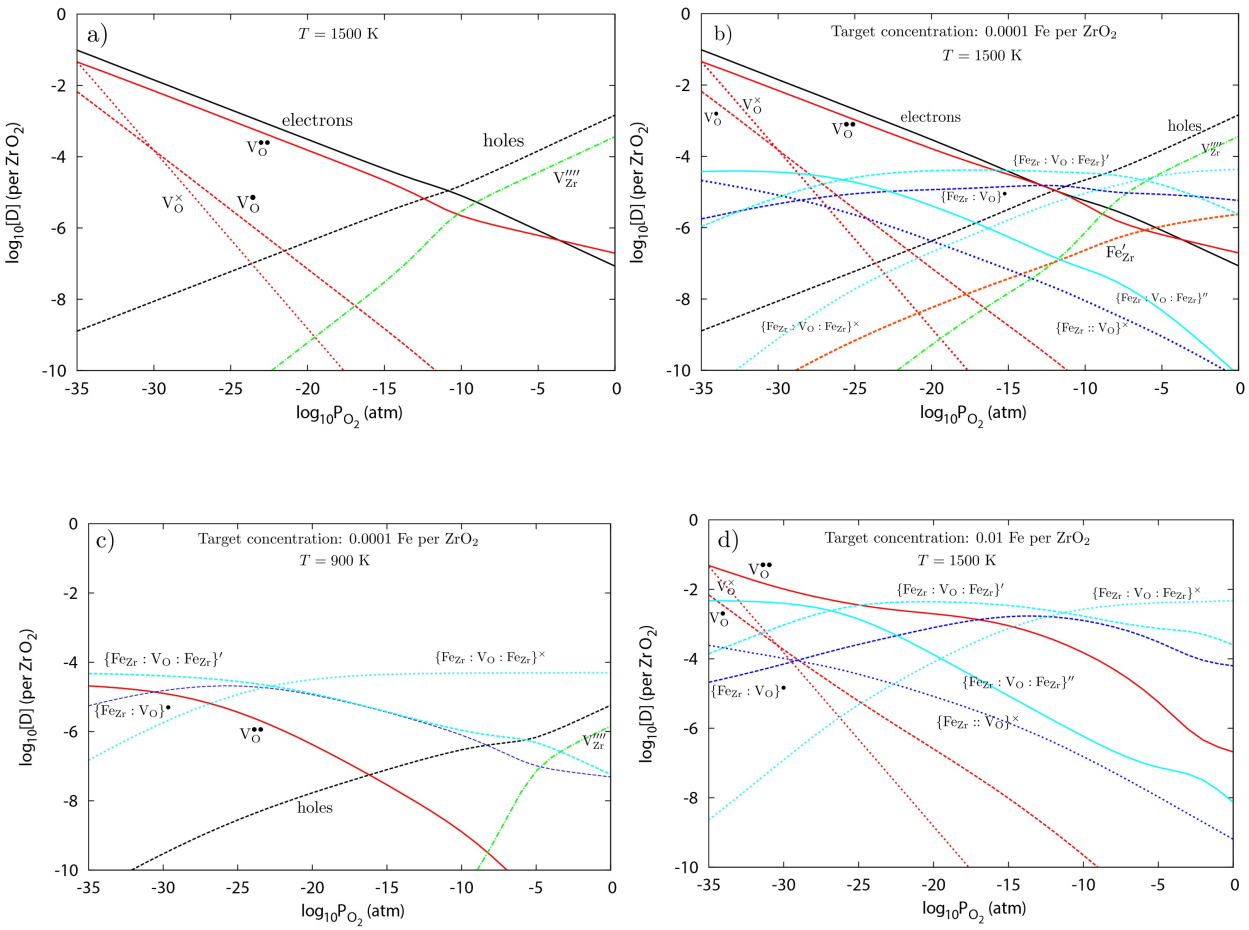

Figure 3: Brouwer diagrams showing defect concentrations in tetragonal ZrO_2 as a function of oxygen partial pressure for a) ZrO_2 with no iron at 1500 K, b) 0.0001 units of iron per ZrO_2 at 1500 K, c) 0.0001 units of iron per ZrO_2 at 900 K and d) 0.01 units of iron per ZrO_2 at 1500 K showing only the oxygen vacancies and paired iron defects. The double colon indicates the oxygen vacancy at a 2nd nearest neighbour site with respect to the iron atom. In all diagrams, defects with concentrations below 10^{-6} at all P_{O_2} are not shown.

The results are in good agreement with previous work reporting DFT simulations of strongly iron-doped (> 1 at.%) oxides in both monoclinic and tetragonal ZrO_2, as well as experimental characterisation of iron-doped ZrO_2 thin films [30]. The study suggested that iron predominantly favours the 3+ state and charge compensates $V_O^{\bullet\bullet}$ at a ratio of two iron atoms to one oxygen vacancy.

3.2 Binding Energies and Relaxation Volumes

Defect cluster binding energies and relaxation volumes are reported in Tables 2 and 3. The clusters generally show positive (favourable) binding energies, which are reflected in the Brouwer diagrams, where clustered defects are favourable (in general) over isolated defects.

Since the binding energies are large in comparison to thermal energies, once a substitutional iron atom is bound to an oxygen vacancy, it is not likely to become unbound. Therefore the presence of iron could effectively immobilise the oxygen vacancies, which further supports the case for iron slowing the movement of O^{2-} through the oxide.

The relaxation volume values help explain why clustering is energetically favourable (though coulomb attraction of charge defects is still the dominant factor). Relaxation volumes of (single) substitutional iron are large and positive. These may be compensated by oxygen vacancies, which have negative relaxation volumes if they cluster together (i.e. the total stresses can be reduced). Iron in the 3+ state also shows a smaller relaxation volume compared to the 2+ state, contributing to the stability of the 3+ oxidation state.

The relaxation volumes also allow us to consider the possible effects of stress in the oxide on defect stability that was not accounted for in the DFT model. It seems likely that in the real oxides, defects with modestly negative relaxation volumes would be slightly more favourable than the Brouwer diagrams suggest if large compressive stresses are present, as is the case (up to 3 GPa) [35, 57].

Table 2 reports that the defect cluster most in evidence in the Brouwer diagram (Figure 2), that is $\{Fe'_{Zr} : {}^{3}V^{\bullet\bullet}_{O} : Fe'_{Zr}\}^{\times}$, has a negative relaxation volume and there is a small reduction in total defect volume when the three defects cluster to form this trimer defect. Thus, the conclusion from the Brouwer diagram that this is the important cluster should hold true in the real (compressed) oxide layer. Indeed the cluster should be evident to slightly higher P_{O_2} values through the small binding energy (compared to other clusters) and the small volume change means that it is not going to be significant compared to isolated Fe'_{Zr} (as in the Brouwer diagram).

Table 3 reports larger positive binding energies for tetragonal ZrO_2 in comparison to the monoclinic phase, which drives the cluster formation observed in the Brouwer diagrams (Figure 3). Considering then the change in defect volume upon clustering, the three trimer defects give rise to volume increases compared to isolated defects. Despite this, the trimer defects are still expected to be dominant (as in the Brouwer diagrams) as defect charges are the main driving force for the clustering. Thus, it is then expected that the formation of these trimers will lead to an increase in the stresses within the oxide, which may in turn result in an earlier onset of cracking in the protective oxide layer.

Table 2: Binding energies, relaxation volumes and clustering volumes of defects in monoclinic ZrO_2 at 635 K and 10^{-2} atm P_{O_2}. Binding energies for clustered defects are calculated from the $V_O^{\bullet\bullet}$ ground state. ^3V_O and ^4V_O refer to vacancies in the 3-coordinated and 4-coordinated oxygen sites respectively.

Defect	Binding energy (eV)	Relaxation Volume (Å^3)	Volume change upon clustering (Å^3)
$\{Fe'_{Zr} : {}^3V_O^{\bullet\bullet} : Fe'_{Zr}\}^{\times}$	1.62	-7.52	-1.33
$\{Fe'_{Zr} : {}^3V_O^{\bullet\bullet} : Fe''_{Zr}\}'$	3.78	6.42	0.98
$\{Fe''_{Zr} : {}^3V_O^{\bullet\bullet} : Fe''_{Zr}\}''$	5.07	19.68	2.61
$\{Fe'_{Zr} : {}^4V_O^{\bullet\bullet} : Fe'_{Zr}\}^{\times}$	-1.85	-14.97	-12.4
$\{Fe'_{Zr} : {}^4V_O^{\bullet\bullet} : Fe''_{Zr}\}'$	0.57	-0.55	-9.61
$\{Fe''_{Zr} : {}^4V_O^{\bullet\bullet} : Fe''_{Zr}\}''$	3.34	16.49	-4.20
$\{Fe'_{Zr} : {}^3V_O^{\bullet\bullet}\}^{\bullet}$	0.59	-17.11	-0.94
$\{Fe''_{Zr} : {}^3V_O^{\bullet\bullet}\}^{\times}$	2.40	-3.90	0.64
$\{Fe'_{Zr} : {}^4V_O^{\bullet\bullet}\}^{\bullet}$	0.67	-13.35	-0.85
$\{Fe'_{Zr} :: {}^4V_O^{\bullet\bullet}\}^{\bullet}$	1.40	-16.00	-3.45
$\{Fe''_{Zr} : {}^4V_O^{\bullet\bullet}\}^{\times}$	0.93	-4.98	-4.06
Fe'_{Zr}	-	9.98	-
Fe''_{Zr}	-	21.61	-
$^3V_O^{\bullet\bullet}$	-	-26.15	-
$^4V_O^{\bullet\bullet}$	-	-22.53	-

Table 3: Binding energies, relaxation volumes and clustering volumes of defects in tetragonal ZrO_2 at 1500 K and 10^{-2} atm P_{O_2}. Binding energies for clustered defects are calculated assuming the oxygen vacancies have a 2^+ charge.

Defect	Binding energy (eV)	Relaxation Volume (Å^3)	Volume change upon clustering (Å^3)
$\{Fe'_{Zr} : V_O^{\bullet\bullet} : Fe'_{Zr}\}^{\times}$	4.05	-3.05	6.51
$\{Fe'_{Zr} : V_O^{\bullet\bullet} : Fe''_{Zr}\}'$	5.42	25.7	17.7
$\{Fe''_{Zr} : V_O^{\bullet\bullet} : Fe''_{Zr}\}''$	5.83	42.9	17.34
$\{Fe'_{Zr} : V_O^{\bullet\bullet}\}^{\bullet}$	2.11	-17.47	5.85
$\{Fe''_{Zr} : V_O^{\bullet\bullet}\}^{\times}$	1.30	-8.82	-3.06
$\{Fe''_{Zr} :: V_O^{\bullet\bullet}\}^{\times}$	2.38	-2.87	2.89
Fe'_{Zr}	-	13.76	-
Fe''_{Zr}	-	31.32	-
$V_O^{\bullet\bullet}$	-	-37.08	-
$V_O^{\bullet}$	-	-19.04	-
$V_O^{\times}$	-	-2.16	-

3.3 XANES

The normalised XANES Fe K-edge spectra for the standards are shown in Figure 4. As expected, the edge energy increases with oxidation state. Note also that the pre-peak feature at $\sim$ 7106 eV (arrowed) appears most strongly in the fully-reduced iron foil XANES spectrum, but is also apparent in the Fe_2O_3 XANES spectrum.

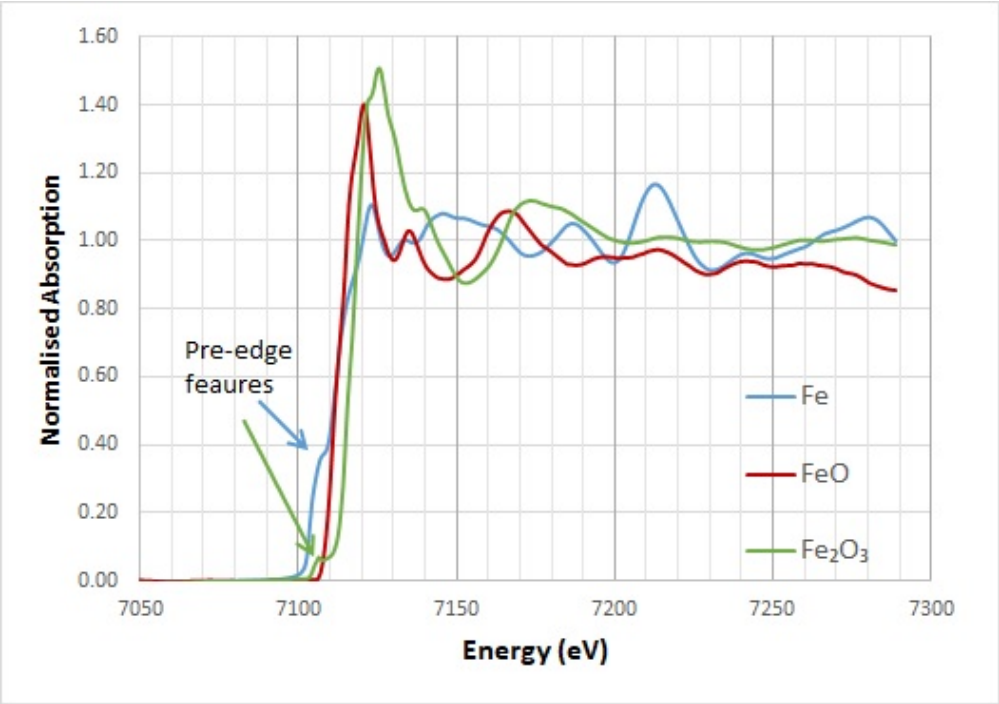

Figure 4: XANES spectra from the Fe foil, FeO and Fe_2O_3 standards. The pre-edge features are indicated.

The normalised iron K-edge XANES spectra for both the metal/oxide interface and the oxide surface in the Zircaloy-4 oxide are shown in Figure 5. The edge energy for the location close to the air-oxide interface was observed to be 7118.4 eV; the same value as that for the Fe_2O_3 standard. The edge energy for the location near the metal-oxide interface was determined to be 7114.4 eV. In both locations the pre-peak feature is clearly apparent.

The linear combination fitting procedure, allowing combinations of all three standards to be fitted to the sample spectra, yielded good fits using just the Fe and Fe_2O_3 XANES data, although slightly better fits could be obtained using spectra from all three standards. The linear combination fits to the data are shown in Figure 6, and the proportions of Fe, FeO and Fe_2O_3 are shown in Table 4.

The fits are consistent with the presence of metallic Fe^0 and Fe^{3+} (with a trace of Fe^{2+}) throughout the oxide. This shows that the SPPs within the oxide were not fully oxidised,

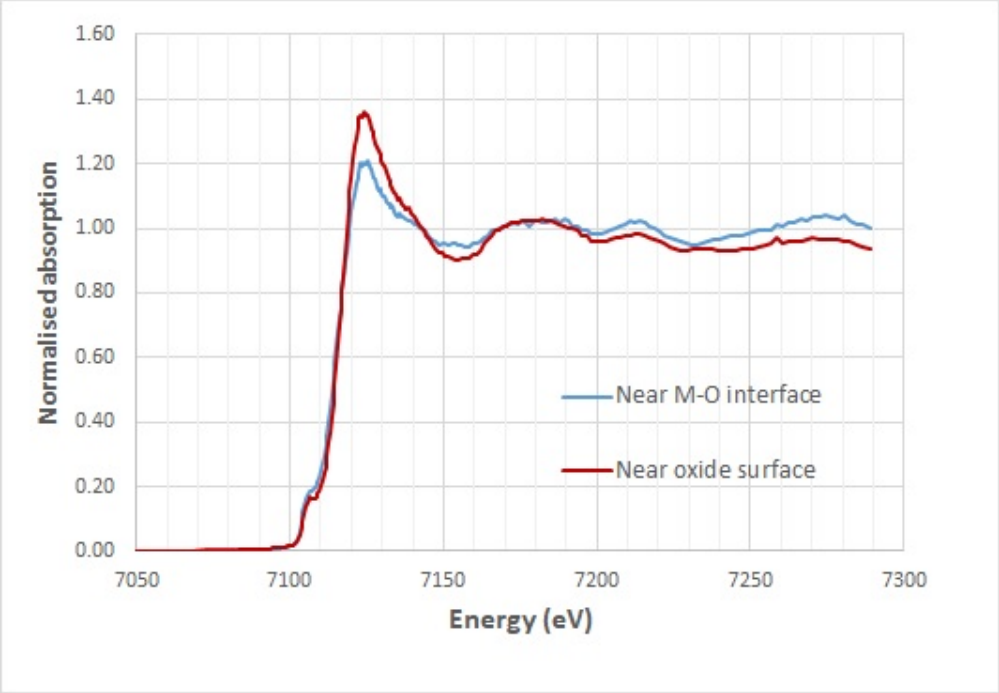

Figure 5: XANES spectra from the two Zircaloy-4 oxide sample locations: near the metal-oxide interface and near the oxide surface.

Table 4: Results of linear combination fitting of standards to XANES data from Zircaloy-4 oxide.

Sample	Fe	FeO	Fe_2O_3	R-factor
Near M/O interface (2 standards)	0.57	-	0.43	0.00338
Near oxide surface (2 standards)	0.33	-	0.67	0.00205
Near M/O interface (3 standards)	0.56	0.02	0.42	0.00336
Near oxide surface (3 standards)	0.27	0.09	0.65	0.00124

even close to the outer surface. The delayed rate of SPP oxidation with respect to the matrix, and the sequential oxidation of the different SPP constituents, have been observed previously [20, 22, 58, 59]. Most recently, Annand *et al.* [60] have illustrated the separation of $Zr(Fe,Cr)_2$ SPPs into metallic Fe^0 clusters and a Zr-Cr oxide in Zircaloy-4 as it oxidises with high-resolution chemical mapping. The oxidation of iron is thermodynamically supported at the oxidation temperature (and at reactor operating temperatures) [61], so the retention of some metallic Fe^0 in the present samples must be a kinetic effect related to the protective

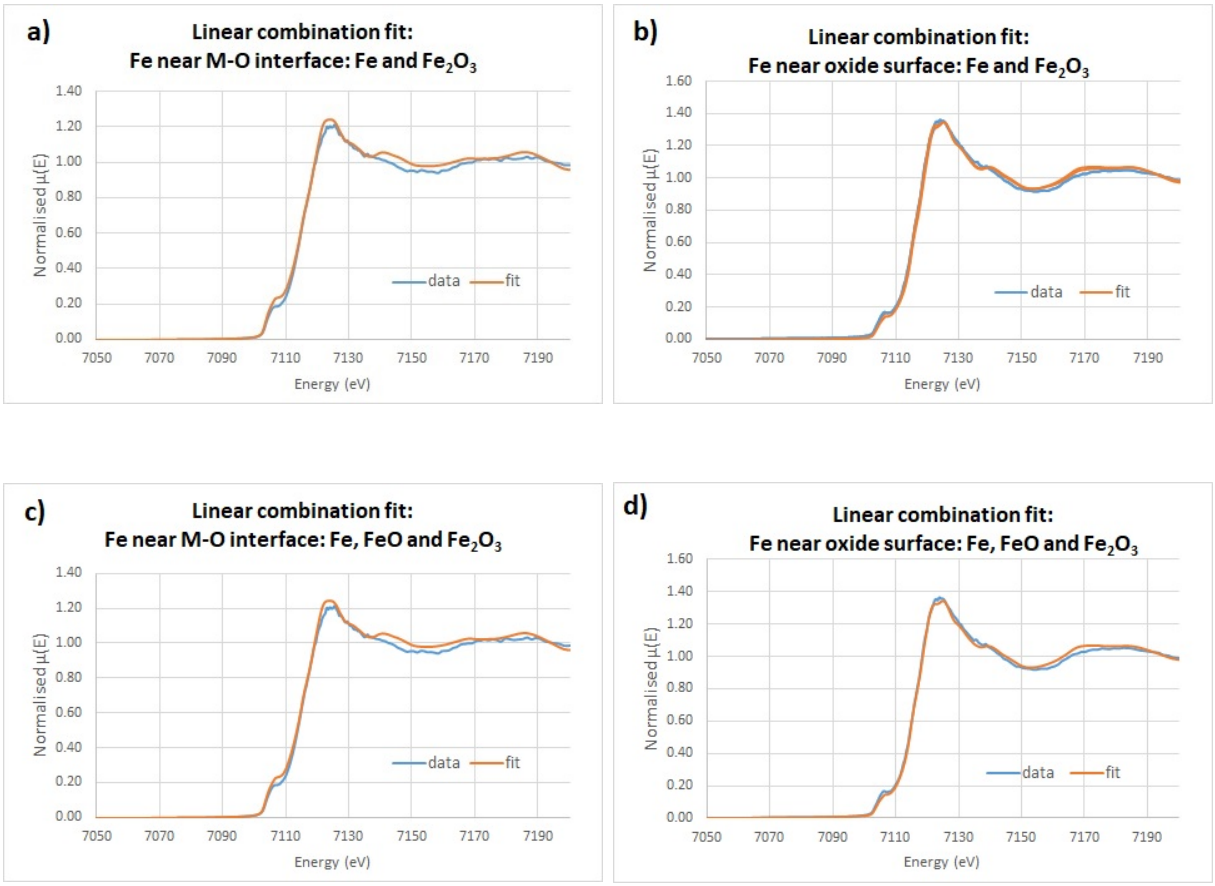

Figure 6: Linear combination fitting results: (a) location near metal-oxide interface (Fe and Fe_2O_3 only), (b) location near oxide surface (Fe and Fe_2O_3 only), (c) location near metal-oxide interface (Fe, FeO and Fe_2O_3), (d) location near oxide surface (Fe, FeO and Fe_2O_3).

nature of the alloy oxides surrounding the clusters and the sizes of some of the iron clusters. The XANES results thus confirm that that iron initially within SPPs does not necessarily oxidise when the mean partial pressure of oxygen at a given depth into the oxide reaches the appropriate level. To the contrary, oxidation and the mixing of cations on the zirconia lattice are both delayed, causing the distribution of iron within the oxide to remain extremely inhomogeneous even in thick oxides. In consequence, it is important to use an applicable local concentration of iron rather than the bulk concentration of iron in simulations.

Where the iron has oxidised, the XANES shows a clear preference for the 3+ oxidation state rather than the 2+ oxidation state, in agreement with the DFT results. The lowering of the average oxidation state of iron between the surface and the metal-oxide interface is also clear. Previous XANES experiments [31,62] have also found that the average fraction of oxidised iron decreases as a function of probe depth into the oxide layer, which agrees with the results presented here.

4 Conclusion

This study has considered the effect of iron doping on monoclinic and tetragonal ZrO_2. It is predicted that in monoclinic ZrO_2, at cladding operating temperatures, iron will exist predominantly as a single 3+ defect, charge compensated by electron holes. As such, iron doping leads to significant increases in the concentration of holes on the oxide layer. As X-ray studies show that, even close to the metal-oxide interface, the major zirconia phase is monoclinic [63], this suggests that the increase in hole concentration due to the presence of iron will likely lead to a build-up of positive charge on the most protective parts of the oxide layer, impeding the inflow of H^+ and thus lowering HPUF.

In tetragonal ZrO_2, at a temperature commensurate with its stable formation, it is predicted that oxygen vacancies will be bound (in a cluster) to one or more iron substitutional species due to the very favourable defect binding energies. The tetragonal oxide is more commonly observed closest to the metal-oxide interface, where the P_{O_2} is lowest [41]. Under these conditions, the 2+ charge state is more common in the tetragonal oxide than in the monoclinic oxide (though bound to an oxygen vacancy). For instance, the simulations predict at the P_{O_2} of 10^{-30} atm, the concentration of Fe^{2+} is about 10^{-4} per ZrO_2 in the tetragonal ZrO_2 while only about 10^{-9} per ZrO_2 in monoclinic ZrO_2. A reduction in the oxidation rate in the presence of iron then supports the link between oxidation rates and oxygen diffusion through the oxide since the main mechanism of oxygen transport in tetragonal ZrO_2 is hopping via oxygen vacancies [64].

XANES analysis confirms the modelling prediction of the dominance of the 3+ state for iron in the bulk oxide formed on Zircaloy-4 cladding. The presence of metallic Fe^0 seen in the XANES data is consistent with the delayed oxidation of the iron that remains undissolved in the bulk oxide such as in the form of SPPs.

The effect of stress in the oxide has been considered by examining relaxation and clustering volumes for different defects and defect clusters. In the monoclinic phase, cluster formation generally leads to a reduction in total defect volume. Compressive stresses, as are found in oxides formed on cladding, will therefore tend to stabilise the vacancy-iron clusters in the monoclinic oxide, possibly encouraging the reduction in oxygen diffusion rates (especially since most of the ZrO_2 is in the monoclinic phase). In the tetragonal phase however, cluster formation generally leads to an increase in defect volume, which may lead to increased stresses within the oxide as clustered defects form.

Acknowledgements

The authors thank Imperial College High Performance Computing Centre for the computational resources provided, as well as the beamline staff at the Diamond Light Source in Oxfordshire for their assistance. Than acknowledges Singapore Nuclear Research and Safety

Institute for the financial support. Bell and Wenman thank National Nuclear Laboratories for the funding of this work. Ortner and Swan acknowledge Amec Foster Wheeler for funding and permission to publish.

References

[1] M. F. Ashby and M. Smidman. Materials for Nuclear Power Systems, 2010.

[2] G. P. Sabol, R. J. Comstock, R. A. Weiner, P. Larouere, and R. N. Stanutz. In-Reactor Corrosion Performance of ZIRLO and Zircaloy-4. In *Zirconium in the Nuclear Industry: Tenth International Symposium*, pages 724–744. ASTM International, 100 Barr Harbor Drive, PO Box C700, West Conshohocken, PA 19428-2959, 1994.

[3] A. T. Motta, M. J. Gomes da Silva, A. Yilmazbayhan, R. J. Comstock, Z. Cai, B. Lai, M. Limback, B. Kammenzind, and S. W. Dean. Microstructural Characterization of Oxides Formed on Model Zr Alloys Using Synchrotron Radiation. *J. ASTM Int.*, 5(3):1–20, 2008.

[4] S. Kass. Hydrogen Pickup in Various Zirconium Alloys during Corrosion Exposure in High-Temperature Water and Steam. *J. Electrochem. Soc.*, 107(7):594–597, 1960.

[5] S. Kass. The Development of the Zircaloys. In *Corrosion of Zirconium Alloys*, pages 3–27. ASTM International, 100 Barr Harbor Drive, PO Box C700, West Conshohocken, PA 19428-2959, 1964.

[6] K. Kakiuchi, K. Ohira, N. Itagaki, Y. Otsuka, Y. Ishii, and A. Miyazaki. Irradiated Behavior at High Burnup for HiFi Alloy. *J. Nucl. Sci. Technol.*, 43(9):1031–1036, 2006.

[7] C. Anghel, G. Hultquist and M. Limback. Influence of Pt, Fe/Ni/Cr-containing intermetallics and deuterium on the oxidation of Zr-based materials. *J. Nucl. Mater.*, 340(2-3):271–283, 2005.

[8] K. Kakiuchi, N. Itagaki, T. Furuya, A. Miyazaki, Y. Ishii, S. Suzuki, T. Terai, and M. Yamawaki. Role of Iron for Hydrogen Absorption Mechanism in Zirconium Alloys. *J. ASTM Int.*, 1(10):1–16, 2004.

[9] Y. Hatano, R. Hitaka, M. Sugisaki and M. Hayashi. Influence of size distribution of $Zr(Fe,Cr)_2$ precipitates on hydrogen transport through oxide film of Zircaloy-4. *J. Nucl. Mater.*, 248:311–314, 1997.

[10] Y. Hatano, M. Sugisaki, K. Kitano, and M. Hayashi. Role of Intermetallic Precipitates in Hydrogen Transport through Oxide Films on Zircaloy. In *Zircon. Nucl. Ind. Twelfth Int. Symp.*, pages 901–917. ASTM International, 100 Barr Harbor Drive, PO Box C700, West Conshohocken, PA 19428-2959, 2000.

[11] D. Hudson and G. D. W. Smith. Initial observation of grain boundary solute segregation in a zirconium alloy (ZIRLO) by three-dimensional atom probe. *Scr. Mater.*, 61(4):411–414, 2009.

[12] B. Gault, P. J. Felfer, M. Ivermark, H. Bergqvist, J. M. Cairney, and S. P. Ringer. Atom probe microscopy characterization of as quenched Zr0.8 wt% Fe and Zr0.15 wt% Cr binary alloys. *Mater. Lett*, 91:63–66, 2013.

[13] A. Couet, A. T. Motta, and R. J. Comstock. Hydrogen pickup measurements in zirconium alloys: Relation to oxidation kinetics. *J. Nucl. Mater.*, 451(1-3):1–13, 2014.

[14] G. P. Sabol and G. D. Moan. *Zirconium in the Nuclear Industry: Twelfth International Symposium*. ASTM International, 100 Barr Harbor Drive, PO Box C700, West Conshohocken, PA 19428-2959, 2000.

[15] F. Stein, G. Sauthoff, and M. Palm. Experimental determination of intermetallic phases, phase equilibria, and invariant reaction temperatures in the Fe-Zr system. *J. Phase Equilib.*, 23(6):480–494, 2002.

[16] D. Hudson, G. D. W. Smith, and B. Gault. Optimisation of mass ranging for atom probe microanalysis and application to the corrosion processes in Zr alloys. *Ultramicroscopy*, 111(6):480–486, 2011.

[17] R. Krishnan and M. K. Asundi. Zirconium alloys in nuclear technology, 1981.

[18] P. A. Burr, M. R. Wenman, B. Gault, M. P. Moody, M. Ivermark, M. J. D. Rushton, M. Preuss, L. Edwards and R. W. Grimes. From solid solution to cluster formation of Fe and Cr in α-Zr. *J. Nucl. Mater.*, 467(Part 1):320–331, 2015.

[19] G. Sundell, M. Thuvander, and H. O. Andrén. Enrichment of Fe and Ni at metal and oxide grain boundaries in corroded Zircaloy-2. *Corros. Sci.*, 65:10–12, 2012.

[20] C. Proff, S. Abolhassani, and C. Lemaignan. Oxidation behaviour of zirconium alloys and their precipitates A mechanistic study. *J. Nucl. Mater.*, 432(1-3):222–238, 2013.

[21] C. Proff, S. Abolhassani, M. M. Dadras, and C. Lemaignan. In situ oxidation of zirconium binary alloys by environmental SEM and analysis by AFM, FIB, and TEM. *J. Nucl. Mater.*, 404(2):97–108, 2010.

[22] C. Proff, S. Abolhassani, and C. Lemaignan. Oxidation behaviour of binary zirconium alloys containing intermetallic precipitates. *J. Nucl. Mater.*, 416(1-2):125–134, 2011.

[23] G. Sundell, M. Thuvander, P. Tejland, M. Dahlback, L. Hallstadius and H.-O. Andren. Redistribution of alloying elements in Zircaloy-2 after in-reactor exposure. *J. Nucl. Mater.*, 454(1-3):178–185, 2014.

[24] M. Griffiths, R. W. Gilbert, and G. J. C. Carpenter. Phase instability, decomposition and redistribution of intermetallic precipitates in Zircaloy-2 and -4 during neutron irradiation. *J. Nucl. Mater.*, 150(1):53–66, 1987.

[25] W. J. S. Yang, R. P. Tucker, B. Cheng, and R. B. Adamson. Precipitates in zircaloy: Identification and the effects of irradiation and thermal treatment. *J. Nucl. Mater.*, 138(2-3):185–195, 1986.

[26] M. Topping, A. Harte, P. Frankel, C. Race, G. Sundell, M. Thuvander, H.-O Andren, D. Jadernas, P. Teiland, J. Romero, E.C. Darby, S. Dumbill, L. Hallstadius and M. Preuss. The Effect of Iron on Dislocation Evolution in Model and Commercial Zirconium Alloys. In *Zircon. Nucl. Ind. Eighteenth Int. Symp.* ASTM International, 100 Barr Harbor Drive, PO Box C700, West Conshohocken, PA 19428-2959, 2016.

[27] A. Harte, M. Topping, P. Frankel, D. Jadernas, J. Romero, L. Hallstadius, E.C. Darby and M. Preuss. Nano-scale chemical evolution in a proton-and neutron-irradiated Zr alloy. *J. Nucl. Mater.*, 487:30–42, 2017.

[28] E. M. Francis, A. Harte, P. Frankel, S. J. Haigh, D. Jadernas, J. Romero, L. Hallstadius, and M. Preuss. Iron redistribution in a zirconium alloy after neutron and proton irradiation studied by energy-dispersive X-ray spectroscopy (EDX) using an aberration-corrected (scanning) transmission electron microscope. *J. Nucl. Mater.*, 454:387–497, 2014.

[29] B. A. van Hassel and A. J. Burggraaf. Oxidation state of Fe and Ti ions implanted in yttria-stabilized zirconia studied by XPS. *Appl. Phys. A Solids Surfaces*, 52(6):410–417, 1991.

[30] D. Sangalli, A. Lamperti, E. Cianci, R. Ciprian, M. Perego, and A. Debernardi. Role of oxygen vacancies on the structure and density of states of iron-doped zirconia. *Phys. Rev. B*, 87(8):085206, 2013.

[31] A. Couet, A. T. Motta, B. De Gabory, and Z. Cai. Microbeam X-ray Absorption Near-Edge Spectroscopy study of the oxidation of Fe and Nb in zirconium alloy oxide layers. *J. Nucl. Mater.*, 452(1-3):614–627, 2014.

[32] K. Kakiuchi, N. Itagaki, T. Furuya, A. Miyazaki, Y. Ishii, S. Suzuki, T. Terai, and M. Yamawaki. Effect of iron on hydrogen absorption properties of zirconium alloys. *J. Phys. Chem. Solids*, 66(2-4):308–311, 2005.

[33] H. J. Beie, A. Mitwalsky, F. Garzarolli, H. Ruhmann, and H. J. Sell. Examinations of the corrosion mechanism of zirconium alloys. *Astm-Stp*, 1245:615–643, 1994.

[34] P. Li, I. W. Chen, and J. E. Penner-Hahn. Effect of Dopants on Zirconia Stabilization — An Xray Absorption Study: III, Charge–Compensating Dopants. *J. Am. Ceram. Soc.*, 77(5):1289–1295, 1994.

[35] E. Polatidis, P. Frankel, J. Wei, M. Klaus, R. J. Comstock, A. Ambard, S. Lyon, R. A. Cottis, and M. Preuss. Residual stresses and tetragonal phase fraction characterisation of corrosion tested Zircaloy-4 using energy dispersive synchrotron X-ray diffraction. *J. Nucl. Mater.*, 432(1-3):102–112, 2013.

[36] P. Platt, P. Frankel, M. Gass, R. Howells, and M. Preuss. Finite element analysis of the tetragonal to monoclinic phase transformation during oxidation of zirconium alloys. *J. Nucl. Mater.*, 454(1-3):290–297, 2014.

[37] P. Platt, R. Mella, W. DeMaio, M. Preuss, and M. R. Wenman. Peridynamic Simulations of the Tetragonal to Monoclinic Phase Transformation in Zirconium Dioxide. *Comput. Mater. Sci.*, 140:322–333, 2017.

[38] B. D. C. Bell, S. T. Murphy, R. W. Grimes, and M. R. Wenman. The effect of Nb on the corrosion and hydrogen pick-up of Zr alloys. *Acta Mater.*, 132:425–431, 2017.

[39] B. D. C. Bell, S. T. Murphy, R. W. Grimes, and M. R. Wenman. The effect of Sn-VO defect clustering on Zr alloy corrosion. submitted, 2017.

[40] S. J. Clark, M. D. Segall, C. J. Pickard, P. J. Hasnip, M. I. J. Probert, K. Refson, and M. C. Payne. First principles methods using CASTEP. *Zeitschrift für Krist.*, 220(5-6-2005):567–570, 2005.

[41] B. De Gabory, A. T. Motta, and K. Wang. Transmission electron microscopy characterization of Zircaloy-4 and ZIRLO oxide layers. *J. Nucl. Mater.*, 456:272–280, 2015.

[42] J. P. Perdew, K. Burke, and M. Ernzerhof. Generalized Gradient Approximation Made Simple. *Phys. Rev. Lett.*, 77(18):3865–3868, 1996.

[43] H. J. Monkhorst and J. D. Pack. Special points for Brillouin-zone integrations. *Phys. Rev. B*, 13(12):5188–5192, 1976.

[44] P. Pulay. Convergence acceleration of iterative sequences. The case of SCF iteration. *Chem. Phys. Lett.*, 73(2):393–398, 1980.

[45] L. Minervini, M. O. Zacate, and R. W. Grimes. Defect cluster formation in M_2O_3-doped CeO_2. *Solid State Ionics*, 116(3):339–349, 1999.

[46] S. Zhang and J. Northrup. Chemical potential dependence of defect formation energies in GaAs: Application to Ga self-diffusion. *Phys. Rev. Lett.*, 67(17):2339–2342, 1991.

[47] S. T. Murphy and N. D. M. Hine. Anisotropic charge screening and supercell size convergence of defect formation energies. *Phys. Rev. B - Condens. Matter Mater. Phys.*, 87(9):1–18, 2013.

[48] G. Makov and M. C. Payne. Periodic boundary conditions in ab initio calculations. *Phys. Rev. B*, 51(7):4014–4022, 1995.

[49] B. D. C. Bell, S. T. Murphy, P. A. Burr, R. W. Grimes, and M. R. Wenman. Accommodation of tin in tetragonal ZrO_2. *J. Appl. Phys.*, 117(8):1–18, 2015.

[50] F. Bruneval, C. Varvenne, J.-P. Crocombette, and E. Clouet. Pressure, relaxation volume, and elastic interactions in charged simulation cells. *Phys. Rev. B*, 91(2):1–8, 2015.

[51] A. Goyal, K. Mathew, R. G. Hennig, A. Chernatynskiy, C. R. Stanek, S. T. Murphy, D. A. Andersson, S. R. Phillpot, and B. P. Uberuaga. The conundrum of relaxation volumes in first-principles calculations of charge defects. arXiv:1704.04044, 2017.

[52] B. Ravel and M. Newville. ATHENA, ARTEMIS, HEPHAESTUS: Data analysis for X-ray absorption spectroscopy using IFEFFIT. *J. Synchrotron Radiat.*, 12(4):537–541, 2005.

[53] W. Weppner. Voltage relaxation measurements of the electron and hole mobilities in yttria-doped zirconia. *Electrochim. Acta*, 22(7):721–727, 1977.

[54] M. Wolf, K. McKenna, and A. Shluger. Hole Trapping at Surfaces of m-ZrO_2 and m-HfO_2 Nanocrystals. *J. Phys. Chem. C*, 116(49):25888–25897, 2012.

[55] M. Youssef and B. Yildiz. Intrinsic point-defect equilibria in tetragonal ZrO_2: Density functional theory analysis with finite-temperature effects. *Phys. Rev. B - Condens. Matter Mater. Phys.*, 86(14):1–14, 2012.

[56] U. Otgonbaatar, W. Ma, M. Youssef, and B. Yildiz. Effect of Niobium on the Defect Chemistry and Oxidation Kinetics of Tetragonal ZrO_2. *J. Phys. Chem. C*, 118(35):20122–20131, 2014.

[57] C. Roy and B. Burgess. A study of the stresses generated in zirconia films during the oxidation of zirconium alloys. *Oxid. Met.*, 2(3):235–261, 1970.

[58] F. Garzarolli, H. Seidel, R. Tricot, and J. P. Gros. Oxide Growth Mechanism on Zirconium Alloys. In *Zircon. Nucl. Ind. Ninth Int. Symp.*, pages 395–415. ASTM International, 100 Barr Harbor Drive, PO Box C700, West Conshohocken, PA 19428-2959, 1991.

[59] D. Pecheur, F. Lefebvre, A. T. Motta, C. Lemaignan, and J. F. Wadier. Precipitate Evolution in the Zircaloy-4 Oxide Layer. *J. Nucl. Mater.*, 189:318–332, 1992.

[60] K. Annand, M. Nord, I. MacLaren, and M. Gass. The Corrosion of $Zr(Fe, Cr)_2$ and Zr_2Fe Secondary Phase Particles in Zircaloy-4 under 350 °C pressurised water conditions. *Corros. Sci.*, 2017.

[61] R. L. Miller and G. A. Reimann. Thermodynamics of gas-metal-slag equilibria for applications in in-situ and ex-situ vitrification melts, 1993.

[62] K. Sakamoto, K. Une, M. Aomi, and K. Hashizume. Depth profile of chemical states of alloying elements in oxide layer of Zr-based alloys. *Prog. Nucl. Energy*, 57:101–105, 2012.

[63] H. Swan, M. S. Blackmur, J. M. Hyde, A. Laferrere, S. E. Ortner, P. D. Styman, C. Staines, M. Gass, H. Hulme, A. Cole-Baker, and R. Frankel. The measurement of stress and phase fraction distributions in pre and post-transition Zircaloy oxides using nano-beam synchrotron X-ray diffraction. *J. Nucl. Mater.*, 479:559–575, 2016.

[64] K. Park and D. R. Olander. Oxygen Diffusion in Single-Crystal Tetragonal Zirconia. *J. Electrochem. Soc.*, 138(4):1154, 1991.